Bulletin of Volcanology (2018) 80:23
https://doi.org/10.1007/s00445-018-1202-8

RESEARCH ARTICLE

Experimental sintering of ash at conduit conditions and implications for the longevity of tuffisites

James E. Gardner[1] · Fabian B. Wadsworth[2] · Edward W. Llewellin[3] · James M. Watkins[4] · Jason P. Coumans[3]

Received: 10 July 2017 / Accepted: 31 January 2018

Abstract

Escape of gas from magma in the conduit plays a crucial role in mitigating explosivity. Tuffisite veins—ash-filled cracks that form in and around volcanic conduits—represent important gas escape pathways. Sintering of the ash infill decreases its porosity, eventually forming dense glass that is impermeable to gas. We present an experimental investigation of surface tension-driven sintering and associated densification of rhyolitic ash under shallow conduit conditions. Suites of isothermal (700–800 °C) and isobaric H_2O pressure (20 and 40 MPa) experiments were run for durations of 5–90 min. Obsidian powders with two different size distributions were used: 1–1600 μm (mean size = 89 μm), and 63–400 μm (mean size = 185 μm). All samples evolved similarly through four textural phases: phase 1—loose and cohesion-less particles; phase 2—particles sintered at contacts and surrounded by fully connected tortuous pore space of up to ~40% porosity; phase 3—continuous matrix of partially coalesced particles that contain both isolated spherical vesicles and connected networks of larger, contorted vesicles; phase 4—dense glass with 2–5% fully isolated vesicles that are mainly spherical. Textures evolve faster at higher temperature and higher H_2O pressure. Coarse samples sinter more slowly and contain fewer, larger vesicles when fully sintered. We quantify the sintering progress by measuring porosity as a function of experimental run-time, and find an excellent collapse of data when run-time is normalized by the sintering timescale $\lambda_s = \eta\overline{R}/\sigma$, where η is melt viscosity, $\overline{R}$ is mean particle radius, and σ is melt–gas surface tension. Because timescales of diffusive H_2O equilibration are generally fast compared to those of sintering, the relevant melt viscosity is calculated from the solubility H_2O content at experimental temperature and pressure. We use our results to develop a framework for estimating ash sintering rates under shallow conduit conditions, and predict that sintering of ash to dense glass can seal tuffisites in minutes to hours, depending on pressure (i.e., depth), temperature, and ash size.

Keywords Sinter · Ash · Tuffisite · Permeability · Diffusion · Hydration

Introduction

Volcanic eruptions often fluctuate between highly explosive emission of ash and pumice, and effusion of lava, all while erupting the same gas-charged magma (Eichelberger et al. 1986; Castro et al. 2012; Schipper et al. 2013). The transition to effusive behavior is thought to result from the escape of magmatic gases, suppressing fragmentation (Eichelberger et al. 1986; Jaupart and Allegre 1991). One mechanism by which gases can escape is magma fracturing in response to shear-induced deformation during ascent (Gonnermann and Manga 2003). Tuffisite veins—ash-filled cracks found in lava flows, volcanic conduits, and Vulcanian blocks—are thought to be remnants of magma fracturing (Stasiuk et al. 1996; Tuffen et al. 2003; Castro et al. 2012).

The efficiency of magma degassing through fractures depends in part on the spacing of fractures and timescale over

Editorial responsibility: J. Dufek

✉ James E. Gardner
gardner@mail.utexas.edu

[1] Department of Geological Sciences, Jackson School of Geosciences, The University of Texas at Austin, Austin, TX 78712-0254, USA

[2] Earth and Environmental Sciences, Ludwig-Maximilians-Universität, Theresienstr. 41/III, 80333 Munich, Germany

[3] Department of Earth Sciences, Durham University, Durham DH1 3LE, UK

[4] Department of Geological Earth Sciences, University of Oregon, Eugene, OR 97403-1272, USA

Published online: 14 February 2018

which the fractures remain open and permeable (Cabrera et al. 2011; Berlo et al. 2013; Castro et al. 2014; Saubin et al. 2016). Diffusive modeling of remnant H_2O concentration gradients next to tuffisites suggests that fractures remain open to gas escape for minutes to tens of hours, depending on the assumed temperature (Cabrera et al. 2011; Castro et al. 2012; Berlo et al. 2013; von Aulock et al. 2013; Saubin et al. 2016). These veins are usually filled with a matrix of juvenile ash, interspersed with vesicular clasts and lithic rock fragments (Tuffen and Dingwell 2005). Deposition of ash in a fracture can clog it and reduce its permeability (Tuffen et al. 2003; Tuffen and Dingwell 2005). Tuffisite veins are often partially to densely welded, with very low porosities (Tuffen et al. 2003; Castro et al. 2014; Saubin et al. 2016), indicating that the ash within them has sintered (Wadsworth et al. 2016a, b). Sintering decreases porosity and permeability of the particle pack, and occurs when viscous particles that share contacts undergo time-dependent coalescence driven by the interfacial tension between the particles and the ambient fluid in the interstitial pore space (Wadsworth et al. 2014, 2016b). Consequently, the time span over which gas can pass through fractures will depend partly on how quickly ash sinters. Shear stresses acting on the particle–particle contacts may accelerate sintering in bulk compaction processes (Michaut et al. 2009; Quane et al. 2009).

Experimental studies have investigated sintering of soda-lime-silica glass beads (Wadsworth et al. 2014, 2016b), synthetic angular glass shards (Vasseur et al. 2013; Wadsworth et al. 2014), and natural tuffisite material (Kendrick et al. 2016). These studies show that melt viscosity and grain size of the starting particle population are important controls on the timescale of sintering. Wadsworth et al. (2016b) found that the characteristic sintering timescale λ_s (s) for randomly packed, monodisperse spherical particles (droplets when molten) is given by

$$\lambda_s = \frac{\eta L}{\sigma} \quad (1)$$

where η is droplet viscosity (Pa s), σ is surface tension (N m^{-1}), and L (m) is a characteristic length scale, which is the particle radius, in the case of incipient sintering, or inter-particle pore radius, in the case of thorough sintering.

All of the experiments referenced above were run at atmospheric pressure, but dissolved H_2O contents indicate that natural tuffisites can form and seal at vapor pressures > 8 MPa (e.g., Castro et al. 2014; Saubin et al. 2016). Importantly, ash in fractures at depth is likely to be relatively rich in H_2O, because H_2O solubility increases with fluid pressure (Blank et al. 1993; Liu et al. 2005), and, in turn, H_2O dissolved in silicate melt strongly lowers viscosity (Hess and Dingwell 1996), implying (from Eq. 1) that λ_s is substantially shorter at depth. The efficiency of degassing via fractures could thus decrease with depth within the conduit. In order to understand better the timescales for sealing tuffisite veins at depth, we have carried out experiments in which ash-sized particles of natural obsidian are sintered in H_2O fluid at high vapor pressures.

Methods

Rhyolitic obsidian that consists of clear rhyolitic glass and less than 1 vol% microlites of Fe–Ti oxides was used in all experiments. The composition of this metaluminous rhyolite has been reported in other studies (e.g., Gardner and Ketcham 2011; Gardner and Webster 2016). Previous work has found that the glass has a dissolved H_2O content of ~0.15 wt% (J. Gardner, unpub. data). The obsidian was crushed into pieces with a steel mortar and pestle, and then those pieces were ground to a powder using an agate mortar and pestle, producing irregular particles (Fig. 1). Some of the powder was sieved before being used in experiments, which we term "sieved"; the remaining portion of the powder was used in "un-sieved" experiments. Splits of each sample were analyzed for their particle size distribution (Fig. 1). We compute the arithmetic weighted mean of the distribution of particle sizes. This is done by computing the weighted sum by $\overline{R} = \sum R_j \xi_j$, where R_j is the jth particle radius bin and ξ_j is the volume fraction of the total particles in that bin. The un-sieved powder has particles that range in size from 1 to ~1600 μm, but large particles are very rare; more than 90% (by volume) of the sample is finer than 200 μm (Fig. 1). Overall, the un-sieved powder has a mean radius ($\overline{R}$) = 89 μm. Grain sizes of the sieved sample are more uniform, with 90% of the sample (by volume) in the 126- to 250-μm size range; overall, $\overline{R}$ = 185 μm. Although there is overlap in sizes between the two samples, half of the un-sieved sample is finer than any of the sieved sample (Fig. 1).

Each experiment consisted of ~30 mg of either sieved or un-sieved powder poured into a Au capsule (3 mm O.D.) that was welded shut on one end. The other end of the capsule was left open. In order to determine starting porosity, separate splits of each powder were poured into cylindrical capsules of known volume and weighed. Assuming a rhyolite density of 2400 kg m^{-3}, the un-sieved powder has a porosity of about 46% and sieved powder has a porosity of about 55%. Slight differences in rhyolite density make little difference in these porosities. The high porosity of the sieved sample relative to the un-sieved sample is qualitatively consistent with the polydispersivity of particle sizes.

Each experimental capsule was placed into a sample holder at the end of an Inconel rod, which was then inserted into a pressure vessel that was fitted with a rapid quench extension, as described in Gardner (2007). The pressure

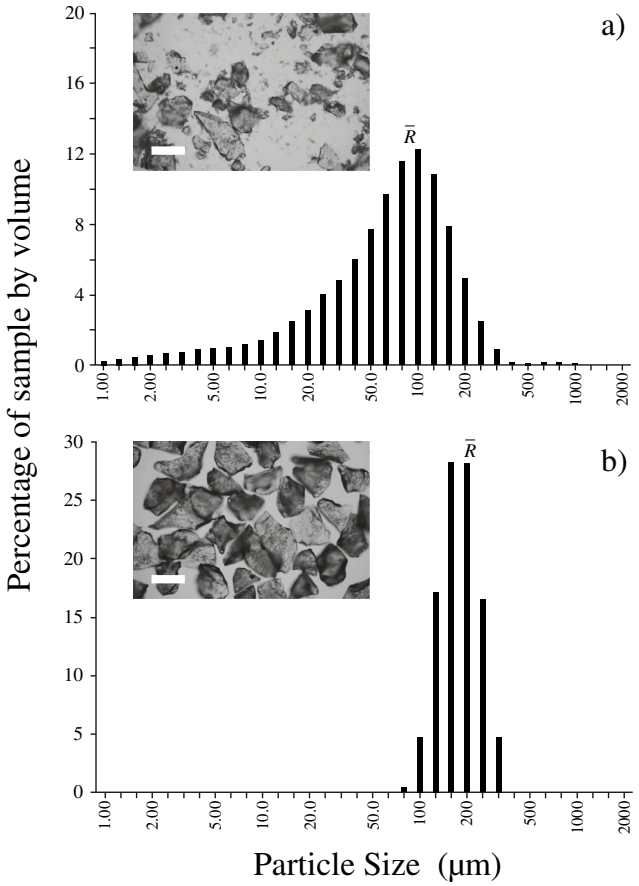

Fig. 1 Particle size distributions of powders used in experiments, with the approximate position of the mean ($\bar{R}$) particle size shown. (a) "Unsieved" powder with sizes from 1 to 1000 μm. (b) "Sieved" powder with a narrower range of sizes. Insets are photomicrographs to illustrate particle sizes and shapes in each. Scale bars are 200 μm long

vessel was connected to the pressure line, and pressure was applied using H_2O (either 20 or 40 MPa). Because the capsule was open at one end, the pressurized H_2O was in contact with the powder, and the pressure in the interstitial open pore space between the particles was equal to that in the pressure vessel. Because pressure inside and outside the capsule was the same, the capsule exerted no stress on the particles within, and the only stress driving sintering resulted from interfacial tension between the molten particles and interstitial H_2O.

An external magnet held the sample rod in place, such that the sample remained inside a water-cooled jacket while the pressure vessel was heated to the desired experimental temperature, as measured using K-type thermocouples precise to ± 5 °C. Pressure was recorded with a pressure transducer precise to ± 0.1 MPa. Once the vessel equilibrated to the desired temperature, the external magnet was raised, lifting the sample into the hot zone of the pressure vessel in ~1 s. Pressure dropped ~2.0 MPa when the sample was raised, but was quickly readjusted to the desired value in ~15 s. The sample was then held in place for 5 to 90 min (Table 1). During that time, pressure varied by no more than 0.1 MPa and temperature varied by no more than 1 °C. After the target time was reached, the magnet was lowered, bringing the sample into the water-cooled jacket where it cooled at ~150 °C per second (Dobson et al. 1989). When the sample was lowered, pressure increased by ~2.0 MPa, but was quickly adjusted back to the experimental pressure in ~15 s.

Samples were extracted from their Au capsules, and, if coherent, sealed in epoxy and thin sectioned to about 500-μm thickness. A petrographic microscope was used to evaluate sample textures and measure vesicle numbers, shapes, and sizes. Porosity was measured by photographing samples in reflected light, and then using NIH *Image* to make binary images of the photographs to measure pore areas relative to the entire area of the image. The area fraction of pores is converted directly to porosity (vol%) under the assumption that the pores are homogeneous throughout the sample and the pore network is isotropic, which is typical of sintering systems without a directional load applied (Wadsworth et al. 2016b). Errors on porosity are estimated at 10% of the measured value. The sizes of vesicles were measured using a graduated ocular on the petrographic microscope. Number density of vesicles (N_v) was measured by selecting different areas in a sample and counting all vesicles that appear as the field of view is moved through it using the focusing knob of the microscope; N_v is thus number density per unit total volume (melt plus vesicles). The depth viewed was measured using a Heidenhain focus drive linear encoder. If more than one type of vesicle occurred in a sample (vesicle types are reported later), each vesicle type was counted and measured separately. All measured textures, porosities, N_v values, and mean vesicle sizes are reported in Table 1.

Area maps of OH, H_2O_m, and total H_2O concentrations were made for four samples using a Thermo Nicolet Nexus 670 Fourier transform infrared (FTIR) spectrometer at the University of Oregon, following the methods of Watkins et al. (2017). All measurements were made using a 15X objective, infrared source, MCT-A detector, and KBr beamsplitter, and absorbances were converted to concentrations using molar absorption coefficients for OH and H_2O_m from Zhang et al. (1997). The thickness of the sample was measured in several spots using a digital caliper with 0.001-mm precision. Run settings for each map were as follows: 100 × 100-μm aperture, step size of 100 μm, spectral resolution of 4 cm^{-1}, 64 scans per spot, and 64 scans for the background, which was collected every 10 min.

Experiments G1664 and G1647 were analyzed using attenuated total reflectance micro-Fourier transform infrared spectroscopy (ATR micro-FTIR). The analyses were performed using a ThermoFisher Nicolet iN10 spectrometer and a Ge crystal at Bristol University (UK). We measured evanescent wave absorption at 1630 and 3450 cm^{-1}, which represent

Table 1 Experimental run conditions and results

Run	T^a (°C)	P^a (MPa)	t^a (min)	ϕ^b (vol%)	$N_v^{(s)c}$ (cm^{-3})	$N_v^{(c)c}$ (cm^{-3})	Size[d] (μm)	H_2O^e (wt%)	Fi[f]	Pe[g]
Un-sieved powder as starting material										
G–1653	700	40	5	–	–	–	–	–	0.2	1.1
G–1664	700	40	15	18.3	–	–	–	2.26 ± 0.25	0.7	1.1
G–1650	700	40	30	15.7	–	–	–	–	1.4	1.1
G–1652	700	40	60	2.4	$10^{6.69}$	$10^{6.25}$	7 ± 8	–	2.9	1.1
G–1657	725	20	5	–	–	–	–	–	0.2	0.5
G–1655	725	20	15	–	–	–	–	–	0.6	0.5
G–1654	725	20	30	38.1	–	–	–	–	1.3	0.5
G–1656	725	20	60	43.6	–	–	–	–	2.6	0.5
G–1647	750	40	5	44.2	–	–	–	1.86 ± 0.25	0.4	2.4
G–1658	750	40	15	8.7	$10^{6.06}$	$10^{5.53}$	5 ± 5	–	1.1	2.4
G–1651	750	40	20	4.7	$10^{6.38}$	$10^{6.02}$	6 ± 4	2.63 ± 0.07	1.5	2.4
G–1646	750	40	30	3.6	$10^{6.49}$	$10^{5.55}$	8 ± 6	–	2.3	2.4
G–1648	750	40	60	5.1	$10^{6.54}$	$10^{4.73}$	18 ± 17	–	4.5	2.4
G–1660	750	40	90	5.5	$10^{6.91}$	–	16 ± 12	–	6.8	2.4
G–1642	800	40	5	31.4	–	–	–	–	0.6	4.8
G–1659	800	40	7	7.0	$10^{6.69}$	$10^{6.14}$	7 ± 5	2.36 ± 0.11	0.8	4.8
G–1649	800	40	10	2.8	$10^{6.55}$	$10^{5.98}$	9 ± 7	2.53 ± 0.09	1.1	4.8
G–1640	800	40	30	2.4	$10^{6.72}$	–	10 ± 16	–	3.4	4.8
G–1641	800	40	60	2.9	$10^{6.46}$	–	13 ± 12	–	6.8	4.8
Sieved powder as starting material										
G–1668	700	40	60	35.2	–	–	–	–	0.7	2.2
G–1669	700	40	90	32.7	–	–	–	–	1.0	2.2
G–1643	750	40	30	25.9	–	–	–	2.45 ± 0.16	0.5 4.9	
G–1667	750	40	45	5.1	$10^{5.47}$	$10^{5.04}$	13 ± 12	–	0.8	4.9
G–1661	750	40	60	1.5	$10^{5.67}$	$10^{5.07}$	17 ± 15	–	1.0	4.9
G–1663	750	40	90	1.9	$10^{5.86}$	$10^{5.20}$	19 ± 13	–	1.6	4.9
G–1666	800	40	10	38.8	–	–	–	–	0.3	9.9
G–1662	800	40	30	2.0	$10^{5.46}$	$10^{4.75}$	20 ± 16	–	0.8	d9.9

[a] Temperature (in °C), pressure (in MPa), and time (in minutes) of the experiment

[b] Vesicularity (in vol%) of the experiment, includes all vesicle types

[c] Number density (in numbers per cm^3) of spherical (s) or contorted (c) vesicles

[d] Average diameter (in μm) of 50 to 200 spherical vesicles

[e] Average dissolved H_2O contents (in wt%) with ± 1-s errors listed

[f] Dimensionless Fick number calculated from Eq. 3, assuming solubility concentrations for H_2O

[g] Dimensionless capillary Peclet number calculated from Eq. 6, assuming solubility concentrations for H_2O and equilibrium viscosity

molecular (H_2O_m) and total water ($H_2O_t = H_2O_m + OH$) species, respectively. An optical aperture of 30 × 30 μm was used with an acquisition time of 25 s, resulting in 128 scans at a spectral resolution of ~10 cm^{-1}. Each analytical point was measured three times, and a new background spectrum was collected before every point. A linear background was applied from 1540 to 1700 cm^{-1} for H_2O_m and 2600–3700 cm^{-1} for H_2O_t. Peak heights and the resulting H_2O species concentration were calculated following the methods and calibration of Lowenstern and Pitcher (2013).

Results

Experiments using un-sieved powder

Overall, the porosities of samples coherent enough to section and measure decreased with time held at experimental temperature (Fig. 2(a)). The highest measured porosities are ~44 vol%, but those samples are incipiently sintered, consistent with an estimated initial porosity of about 45%.

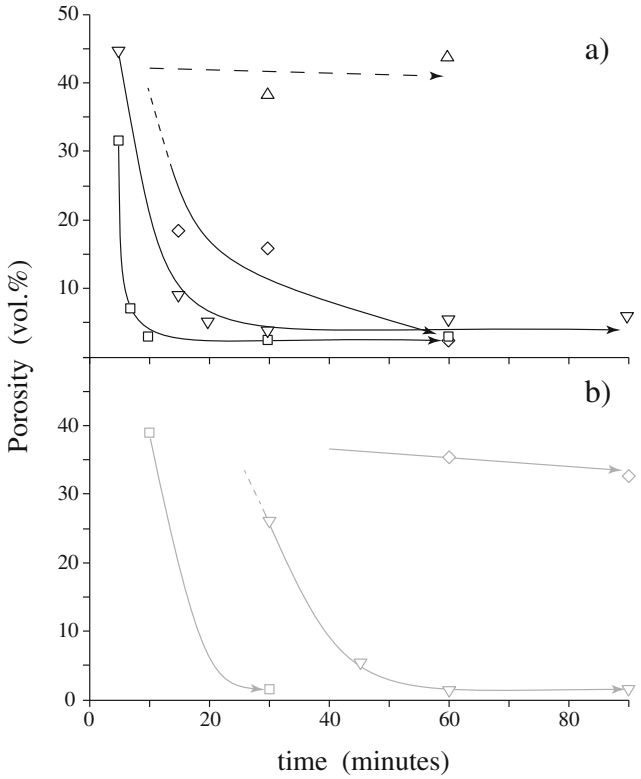

Fig. 2 Porosity (vol%) of sintered samples of (a) un-sieved and (b) sieved obsidian powder as a function of time (errors on porosity are ~10% of measured value): open squares for 800 °C and 40 MPa, inverted triangles for 750 °C and 40 MPa, diamonds for 700 °C and 40 MPa, and triangles for 725 °C and 20 MPa. Sieved samples are in gray. Lines are to guide the eye only

Five experiments were run at 800 °C and 40 MPa for 5–60 min (Table 1). After 5 min, the sample was sufficiently sintered that it held together while it was extracted from the capsule and sectioned. Individual particles are, however, still clearly distinguishable (Fig. 3(a)). The particles are surrounded by an open, porous network that makes up ~30 vol% of the sample (Fig. 3(b)). After 7 min, porosity had dropped to only 7 vol%, but individual particle shapes are still discernable in some cases (Fig. 3(c, d)). Many vesicles are contorted, up to 500+ μm long, and retain the multicuspate shapes that are a feature of the initial inter-particle pore space. Many other vesicles are spherical, and on average ~7 μm in diameter. Spherical vesicles are isolated from their neighbors. Contorted and spherical vesicles occur in roughly equal number densities (Table 1). By 10 min, the sample takes on the appearance of solid glass with vesicles dispersed in it, and the initially separate glass particles can only be discerned optically by differences in original microlite content; porosity dropped to 2.8 vol% and the contorted vesicles are typically approximately 50–200 μm long. Samples held longer than 10 min also appear to be solid pieces of glass (Fig. 3(e, f)), with similar porosities. Spherical vesicles occur throughout, but contorted vesicles decrease substantially in number, and are absent for run times > 10 min (Table 1). The average size of spherical vesicles increases with time, with the largest one observed being ~50 μm at 60 min. This does not imply that the spherical vesicles grew with time; instead, the increase in sizes results from the slow relaxation of larger vesicles from contorted to spherical shape, at which point they contribute to the spherical vesicle population.

Six experiments were run at 750 °C and 40 MPa for 5–90 min (Table 1). The same progression in textural changes is found at these conditions as was found at 800 °C, except that the changes took longer to evolve. Overall, porosity decreased from 44 vol% at 5 min to ~5 vol% at 90 min (Fig. 2(a)). Individual particles are discernable even after 15 min, and it is not until 20 min that samples appear to be solid glass with isolated vesicles dispersed in it. Isolated spherical vesicles formed by 15 min, but contorted vesicles persist for more than 60 min. The number of contorted vesicles decreases with time, while spherical vesicles increase in both number and size (Table 1).

Four experiments were run at 700 °C and 40 MPa for 5–60 min (Table 1). After 5 min, the sample had not sintered enough to hold together, and so it crumbled when removed from the capsule. After 15 min, sintering had progressed sufficiently to hold the sample together, but outlines of individual particles are easily seen and they are partially surrounded by a fully interconnected vesicle network that makes up ~18 vol% of the sample (Fig. 2(a)). After 30 min, outlines of individual particles are difficult to discern, but vesicles remain mainly interconnected, and make up about the same fraction of the sample as after 15 min. Only after 60 min did the sample appear to be solid glass with about 3 vol% vesicles in it. Most vesicles, however, are still contorted in shape, and thin connections between neighboring vesicles are common.

Four experiments were run at 725 °C and 20 MPa for 5–60 min (Table 1). Even after 15 min, samples crumbled when removed from the capsule or during polishing. The sample that ran for 30 min was friable but partly held together when polished. It consists of individual particles that are only slightly sintered, separated by an open network of vesicles that make up ~38 vol% of the sample (Fig. 2(a)). After 60 min, particles appear only slightly more sintered, making a slightly more cohesive sample, although vesicles are all interconnected and still occupy ~40 vol% of the sample.

Experiments using sieved powder

All experiments with sieved powder were run at 40 MPa. As with the un-sieved powder, the porosities of samples decreased with time held at experimental temperature (Fig. 2(b)). Textures of the final products evolved similarly as in the un-sieved samples, but at different rates. Compared to un-sieved samples run under the same conditions, at similar times, vesicles are fewer (lower N_v) and larger (Fig. 4).

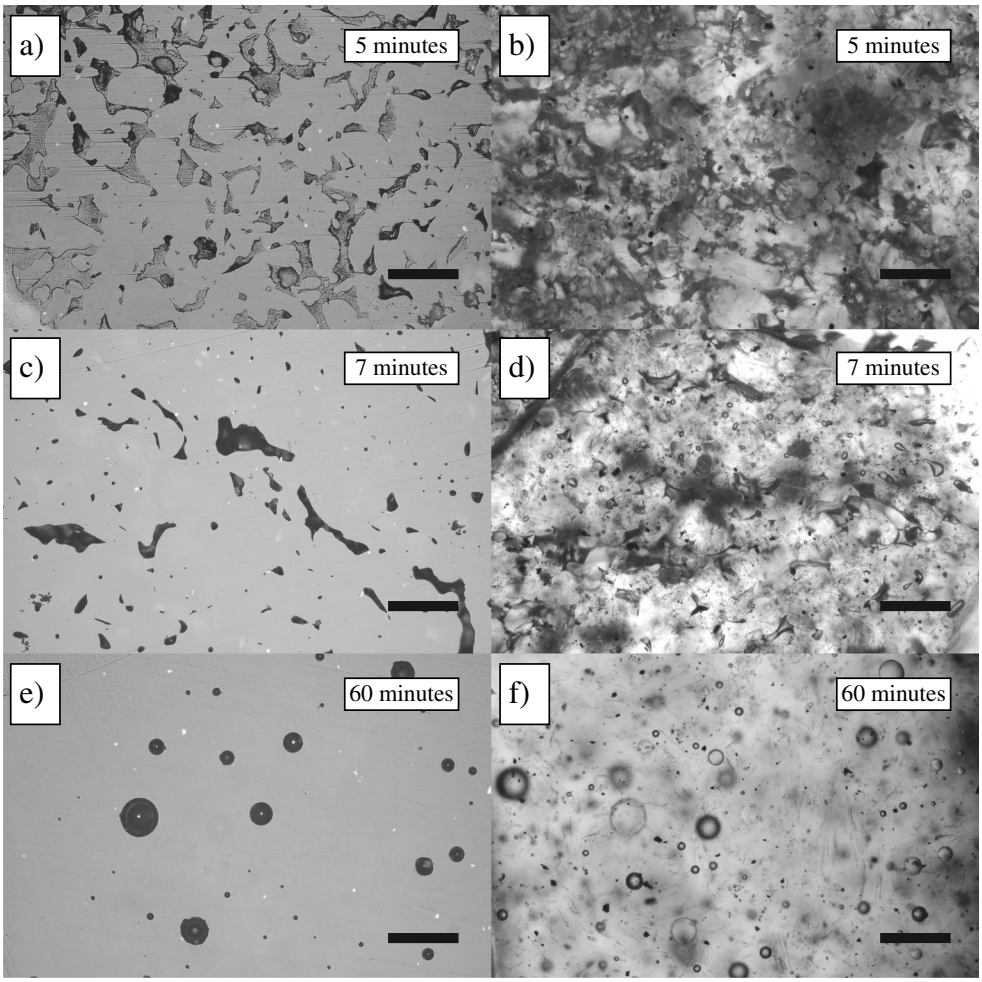

Fig. 3 Photomicrographs showing textures of sintered unsieved ash at 800 °C (scale bars are 200 μm long). (a, b) Individual particles still visible amongst the tortuous, porous network after 5 min (reflected and transmitted light images of G–1642). (c, d) Individual particles still visible, but porosity has decreased significantly after 7 min (reflected and transmitted light images of G–1659). (e, f) Dense glass with low porosity of only spherical vesicles after 60 min (reflected and transmitted light images of G–1641)

Two experiments were run at 800 °C for 10 and 30 min (Table 1). After 10 min, particles have sintered with an interconnected network of vesicles between them. After 30 min, all vesicles are isolated from their neighbors, but many are elongate in shape, rather than spherical (Fig. 4(a)). Four experiments were run at 750 °C for 30–90 min (Table 1). Vesicle textures evolve from an interconnected network at 30 min to isolated vesicles in dense glass at 60 min (Fig. 4(c)). After

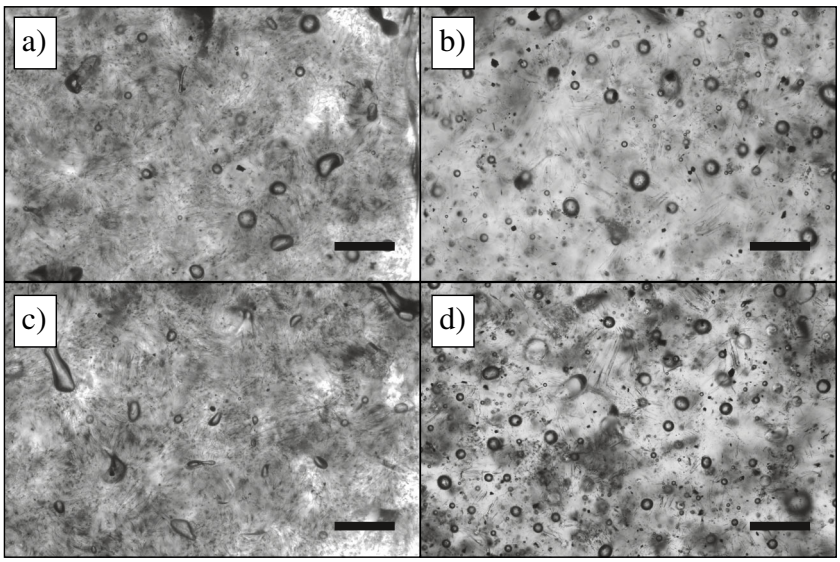

Fig. 4 Photomicrographs showing the differences in textures resulting from sintering of sieved ash (a, c) versus unsieved ash (b, d) at 40 MPa (scale bars are 200 μm long). (a, b) 800 °C for 30 min. (c, d) 750 °C for 60 min

45 min, vesicles are still contorted and occur in clusters in which they are locally connected to their neighbors by thin channels. Clusters are isolated, however, from neighboring clusters. Many vesicles are still contorted in shape, despite occupying only ≤2 vol% of the sample (Fig. 4(c)). Finally, two experiments were run at 700 °C for 60 and 90 min (Table 1). A fully open interconnected network of vesicles persisted after 90 min. Individual particles can still be discerned, although some of their contacts had melded together by 60 min.

H_2O contents

H_2O contents were mapped in four samples using transmission FTIR (G–1659, G–1643, G–1651, and G–1649). In all four, the distribution of H_2O is relatively homogeneous, except where an analysis intersected large vesicles (Fig. 5). Compared with the majority of analyses, these analyses tend to be anomalously low in H_2O contents. Interestingly, we found that the speciation of H_2O associated with these anomalously low H_2O contents corresponds to relatively slow cooling rates (Q), using the method of Zhang et al. (1997). In contrast, analyses that did not intersect vesicles give Q > 10 K s^{-1}, in agreement with the known cooling rate of the experiment. We thus assume that any analysis that gives Q < 10 K s^{-1} is an analytical artifact resulting from intersecting vesicles, and hence exclude that analysis. By averaging only those analyses for which speciation indicates Q > 10 K s^{-1}, we found H_2O contents of 2.4–2.6 wt% (Table 1), in good agreement with H_2O contents expected from solubility (Liu et al. 2005).

H_2O contents of two samples (G–1664 and G–1647) were measured using ATR-FTIR. These analyses are restricted to the surface of the sample, and thus vesicles below the surface should not interfere. Overall, we found average H_2O contents of 2.26 ± 0.25 wt% and 1.86 ± 0.25 wt%, respectively, for G–1664 and G–1647 (Table 1). The larger errors probably result from far fewer analyses per sample, compared to the FTIR maps (n = 11–17 versus 170–239). These values are relatively low, compared with H_2O contents expected from solubility (Liu et al. 2005).

Discussion

The evolution of textures through the sintering process is similar in all sample suites. For convenience, we divide the evolution into four phases, but note that the progression between phases is continuous rather than discrete:

Phase 1—Particles are loose and cohesionless.
Phase 2—Coherent but friable framework of still-discernable particles sintered at their contacts, interpenetrated by a continuous, tortuous pore space of up to ~40% (Fig. 3(a, b)).
Phase 3—Relict particle shapes still present, but porosity is ≤10% and no longer fully connected. Small isolated vesicles are spherical, but networks of larger vesicles remain multi-cuspate in shape (Fig. 3(c, d)).
Phase 4—Dense glass with 2–5% fully isolated vesicles that are mainly spherical; a few larger vesicles can be more complex in shape (Fig. 3(e, f); Fig. 4).

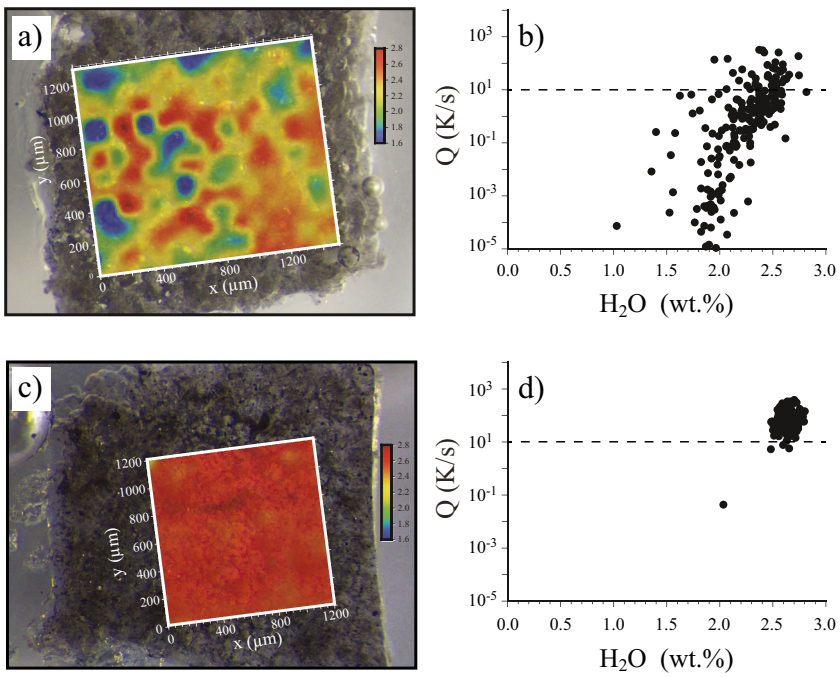

Fig. 5 Apparent dissolved H_2O concentrations and estimated quench rates (Q in K s^{-1}) for two samples. (a, b) G–1643. (c, d) G–1651 (see Table 1 for experimental conditions). H_2O was measured by transmission FTIR. Q is calculated from the speciation of dissolved H_2O (see text). Low apparent H_2O contents and slow Q (<10 K s^{-1}) are artifacts due to analyses intersecting large vesicles. Area maps were processed using Generic Mapping Tools (GMT) software (Wessel et al. 2013). The step size for maps is 100 μm and the aperture size is 100 μm. To make smoothed area maps, we make a subgrid with 10-μm spacing and interpolate values between the measured spots

Our results show that sintering progresses more rapidly at higher temperature at a given pressure; un-sieved particles at 800 °C reached Phase 4 in ≤ 15 min, but at 700 °C did not reach Phase 4 within the 60 min duration of this experiment. In addition, sintering progressed more slowly at 725 °C and 20 MPa than it did at 700 °C and 40 MPa, suggesting that lowering the pressure (i.e., decreasing H_2O_t) had a stronger influence than raising the temperature. Finally, sieved samples, with a larger mean particle size, progress through the phases more slowly under the same conditions (Fig. 2).

Equation 1 and the analysis that underpins it indicate that the sintering timescale, λ_s, is proportional to viscosity of the sintering particles (differences in surface tension are small for the ranges in dissolved H_2O content and temperature of our experiments and so we use an approximate value of surface tension of 0.22 N m^{-1} throughout; Bagdassarov et al. 2000; Gardner and Ketcham 2011). Consequently, we infer that the variations in the rate of progress across the sintering phases resulted primarily from differences in melt viscosity. The two main variables that differ between experiments are temperature and pressure. Temperature directly controls viscosity through its effect on the mobility of network-forming cations Si and Al (Richet 1984; Hess and Dingwell 1996; Giordano and Dingwell 2003; Russell et al. 2003; Giordano et al. 2008). Additionally, temperature and pressure indirectly affect viscosity through their control on the H_2O content of the melt (cf. Liu et al. 2005), which, in turn, directly impacts melt viscosity (e.g., Hess and Dingwell 1996). Assuming that the particles have dissolved H_2O contents equal to the equilibrium solubility (tested in the next subsection), we estimate that the viscosity (which we term η_e at equilibrium solubility) of samples held at 40 MPa and at 700°, 750°, and 800 °C would be $\eta_e \approx 10^{7.1}$, $10^{6.5}$, and $10^{6.0}$ Pa s, respectively, using the model of Hess and Dingwell (1996). We use that model because it is specifically calibrated for metaluminous rhyolite similar to the rhyolite used in our experiments. Those held at 20 MPa and 725 °C should be the most viscous, with $\eta_e \approx 10^{7.5}$ Pa s.

The direct control of melt viscosity on the progression of sintering is apparent when changes in texture are considered as functions of time (Fig. 6). Samples with $\eta_e \approx 10^{7.5}$ Pa s remain in Phase 1 conditions for ~30 min, but for less than 5 min at $\eta_e < 10^{7.0}$ Pa s. Fully closed porosity (Phase 4) is reached in less than 10 min at $\eta_e \approx 10^{6.0}$ Pa s, but takes ~25 min at $\eta_e = 10^{6.5}$ Pa s, and is not reached by 60 min at $\eta_e > 10^{6.5}$ Pa s. In addition, final stable porosities of ~2–5 vol% are reached in 10 min at $\eta_e \approx 10^{6.0}$ Pa s, 20 min at $\eta_e \approx 10^{6.5}$ Pa s, and 60 min at $\eta_e \approx 10^{7.0}$ Pa s (Fig. 2).

The competition between the rates of hydration and sintering is expected to be important for sintering behavior. If hydration is slow compared with sintering, we expect the particles to maintain their initial H_2O content through the sintering process, and hence the controlling viscosity will be that given by the initial H_2O content and temperature. Given that textures evolved more slowly at lower pressure despite a higher temperature, this seems unlikely. If, instead, hydration is fast compared with sintering, we expect the particles to reach their equilibrium solubility H_2O contents early in the

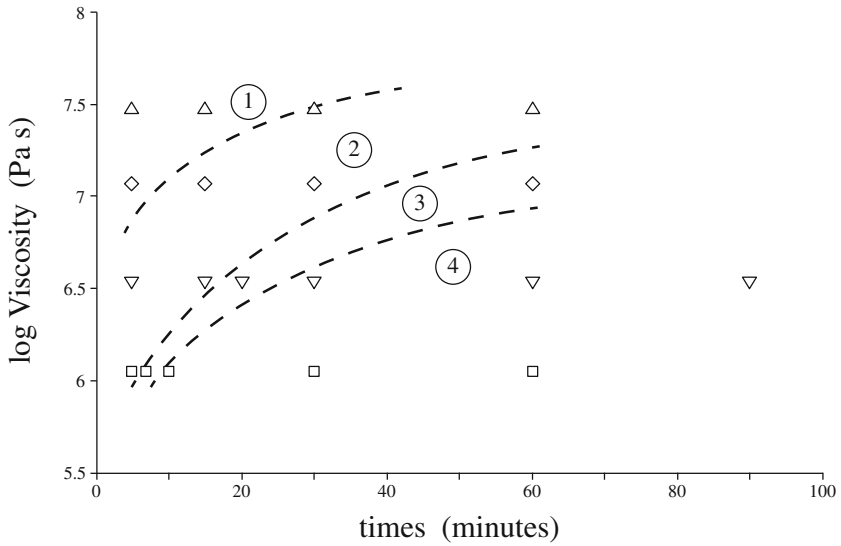

Fig. 6 Variations in sintering texture of un-sieved samples as a function of equilibrium melt viscosity, η_e (calculated at equilibrium H_2O solubility C_e following Liu et al. 2005 and Hess and Dingwell 1996) and experimental time. Symbols are the same as those in Fig. 2. Dashed lines separate approximate fields of constant texture. In Phase 1, individual particles remain loose and lack cohesion. In Phase 2, particles are sintered only at their contacts and porosity is fully open; the sample at 30 min and $\eta_e = 10^{7.5}$ Pa s only partly held together, and was thus at the boundary between Phases 1 and 2. In Phase 3, particles are nearly merged together and the porous texture is nearly sealed, but many vesicles are still multi-cuspate shaped. In Phase 4, samples consist of dense glass with isolated vesicles

sintering process, and hence the controlling viscosity will be that given by the solubility H_2O content. To explore this in more detail, we now compare the expected timescale of ash hydration during the experiments with the timescale of sintering.

Timescale of hydration

The obsidian glass has an initial water content of 0.15 wt%, which is lower than the equilibrium H_2O solubility expected at the experimental conditions (Liu et al. 2005). This means that particles are undersaturated at the start of the experiments, and will hydrate as H_2O progressively dissolves and diffuses into them. Hydration will advance from rim to core over time, resulting in a time-dependent spatial gradient of viscosity, with lower viscosity at the rim, and higher viscosity in the core. Furthermore, small particles are expected to hydrate more rapidly than large particles. We now test the assumption, made earlier, that particles are fully hydrated during the course of the experiments.

Hydration is diffusion-limited, such that there is a characteristic timescale over which the H_2O content of the particles approaches equilibrium with the H_2O solubility at experimental conditions. This hydration timescale λ_d is given by

$$\lambda_d = \frac{\overline{R}^2}{D} \tag{2}$$

where D is diffusivity of H_2O in the silicate melt. We can estimate whether a particle is expected to be fully hydrated by comparing the hydration timescale with the time t for which the particle is held at experimental conditions. The ratio of these timescales gives the dimensionless Fick number (Fi):

$$\mathrm{Fi} = \frac{t}{\lambda_d} = \frac{Dt}{\overline{R}^2}. \tag{3}$$

For $\mathrm{Fi} \gg 1$, hydration is expected to be complete; for $\mathrm{Fi} \ll 1$, hydration is expected to be negligible; and for Fi on order of one, particles are expected to be partially hydrated. We note, however, that a scaling analysis of this sort cannot be used ab initio to predict the value of Fi that divides the hydrated and undersaturated regimes—that requires empirical data.

In order to compute λ_d, and hence Fi, for a specific experiment, we must first calculate diffusivity, which depends on pressure, temperature, and dissolved water concentration. We use the empirical law for diffusivity of total water of Zhang and Ni (2010), which is calibrated for rhyolite over the range of conditions under consideration:

$$D = C \exp\left[a_1 + a_2 P - \left(\frac{a_3 + a_4 P}{T}\right)\right] \tag{4}$$

where C is dissolved water content of the melt in wt%, P and T are in MPa and K, respectively, and $a_1 = -18.1$, $a_2 = 1.888 \times 10^{-3}$, $a_3 = 9699$, and $a_4 = 3.626$ are constants. Our experiments are run under isothermal and isobaric conditions, hence D depends only on C during the experiment. The H_2O concentration at equilibrium solubility, C_e, in the absence of other volatile species, is given by (Liu et al. 2005):

$$C_e = \frac{b_1 P^{0.5} + b_2 P - b_3 P^{1.5}}{T} + b_4 P^{1.5} \tag{5}$$

where $b_1 = 354.941$, $b_2 = 9.623$, $b_3 = 1.5223$, and $b_4 = 0.0012439$ are empirical constants.

Figure 7 plots the measured dissolved water concentrations against those expected at equilibrium solubility, calculated from Eq. 5, with diffusivity calculated at equilibrium solubility via Eqs. 4 and 5. The four samples for which $\mathrm{Fi} > 1$ lie very close to the 1:1 line, indicating that the assumption of full hydration is valid for those samples. The two samples for which $\mathrm{Fi} < 1$ have measured water concentrations slightly lower than the equilibrium value, indicating that these samples are not fully hydrated. The success of this analysis indicates that Fick number is an effective measure of the degree of hydration, and that the boundary between hydrated and undersaturated regimes is indeed near $\mathrm{Fi} = 1$ when using the water concentration at equilibrium solubility instead of the initial water concentration. Fick numbers have been calculated for all experiments, assuming equilibrium H_2O concentrations (Table 1). Fi is close to or greater than 1 for most, implying that the particles in most of the samples can be considered completely hydrated on the timescales of the experiments.

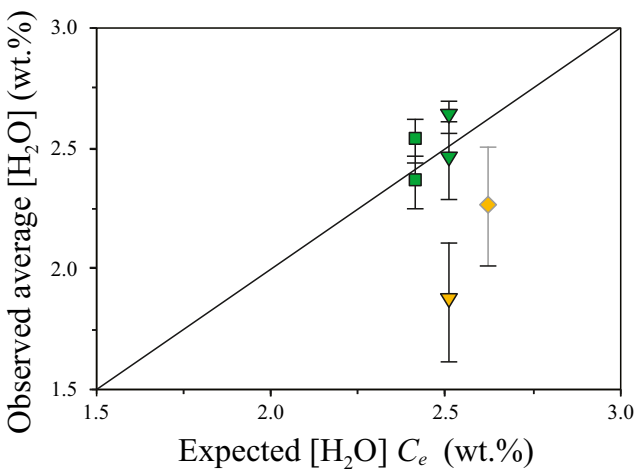

Fig. 7 Observed ($\pm 1\sigma$ errors) versus expected H_2O concentrations for samples at 40 MPa. Symbols are those used in Fig. 2. Solid line is 1:1 line. Samples in green are those for which Fick number $\mathrm{Fi} > 1$ (Eq. 3), indicating complete hydration by the end of the experiment. Samples in yellow are samples for which $\mathrm{Fi} < 1$, indicating incomplete hydration

Modeling sintering of ash particles at elevated vapor pressure

The ratio of sintering and diffusion timescales gives a dimensionless capillary Peclet number (Wadsworth et al. 2017a)

$$\mathrm{Pc} = \frac{\lambda_d}{\lambda_s} = \frac{\sigma \overline{R}}{\eta D}. \quad (6)$$

Note that this formulation includes the implicit assumption that the length scale in Eq. 1 is taken as the particle radius. The capillary Peclet number is of use when we must consider whether time-dependent changes in η or D will have a significant impact on the sintering process. When $\mathrm{Pc} \gg 1$, diffusion is slow compared with sintering, in which case, the time-dependent mass transfer of water and resultant changes in D and η can be neglected, and sintering will be governed by the initial water content C_i and the associated viscosity η_i. When $\mathrm{Pc} \ll 1$, diffusion is fast compared with sintering, in which case time-dependent changes in η or D can again be neglected, but sintering will be controlled by the solubility value of water C_e and the associated viscosity η_e. For intermediate values of Pc, time-dependent changes may be important and should be accounted for in any modeling analysis. As was the case for the Fick number, this scaling analysis cannot be used ab initio to predict the value of Pc that divides the regimes.

We use Eqs. 4 and 5 to find D at equilibrium solubility, and the model of Hess and Dingwell (1996) to calculate the associated η_e for each set of experimental P, T conditions, and then calculate Pc via Eq. 6. We find capillary Peclet numbers in the intermediate range ($0.25 < \mathrm{Pc} < 9$), indicating that further investigation is required to determine into which regime our experiments fall. We do this by comparing our experimental data with the sintering model of Wadsworth et al. (2014), who showed that the porosity of a sintering pack of angular glass particles evolves over time according to the equation

$$\phi = \phi_i \exp\left[-\frac{3t}{2\lambda_s}\right], \quad (7)$$

where ϕ is volume fraction of vesicles, and ϕ_i is the initial volume fraction of vesicles before sintering begins, which was set to either 0.45 or 0.55, based on our measured initial porosities. This model has been shown to give a good approximation to a full sintering model (Wadsworth et al. 2016b) and is used for convenience because of its analytical tractability.

We model the evolution of porosity through sintering under two scenarios: (1) λ_s in Eq. 7 is calculated (Eq. 1) using η_i, which is equivalent to assuming that $\mathrm{Pc} \gg 1$; (2) λ_s is calculated using η_e, which is equivalent to assuming that $\mathrm{Pc} \ll 1$. Curves are plotted for each scenario in Fig. 8, in which we normalize the experimental times by the appropriate λ_s to yield a dimensionless time. We find poor agreement between the predicted evolution of porosity (Eq. 7) and the experimental data scaled according to scenario (1) (Fig. 8(a)). In contrast, there is much better agreement with scenario (2) (Fig. 8(b)). This argues that the experiments fall in the low capillary Peclet number behavioral regime, despite having values of Pc near unity. This is important, because it demonstrates that our experiments faithfully model behavior at equilibrium conditions at elevated pressure and temperature.

Although our experiments dominantly capture behavior in the low capillary Peclet regime, there is some evidence of behavior that would be expected at intermediate capillary Peclet number. A manifestation of progressive hydration is that the rims of particles reach low viscosity and become mobile before the particle interiors. This means that particle contacts can weld together before wholesale sintering takes place, resulting in samples reaching Phase 2 relatively quickly, but individual particle shapes remaining discernable for extended periods of time. Furthermore, small particles hydrate more rapidly than large particles, allowing them to fill in gaps between larger particles, leading to the formation of spherical vesicles relatively early in the sintering process (Phase 2), while larger, contorted vesicles take much longer to become spherical. The absence of small, hydrated particles in the

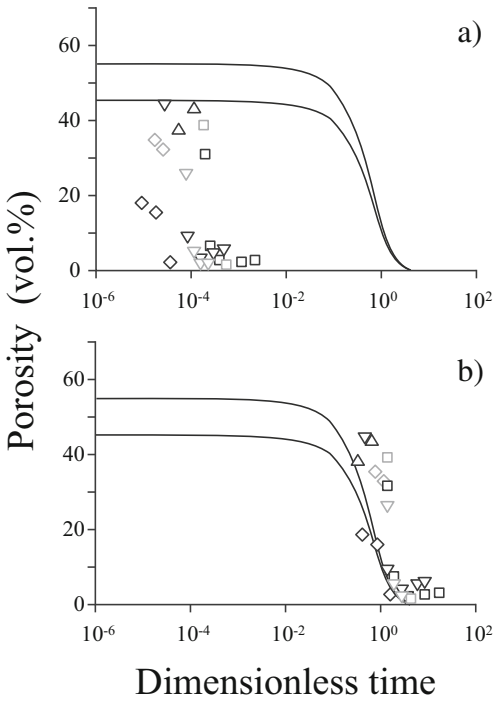

Fig. 8 Model results for sintering of particles, shown as variations in porosity ($\phi \times 100$; Eq. 7), assuming (a) initial (dry) H_2O contents yielding viscosities η_i, or (b) equilibrium H_2O solubility contents yielding viscosities η_e; symbols are the same as Fig. 2. Curves are calculated from Eq. 7. Time is normalized by estimated sintering timescales

sieved samples explain why they took longer to texturally evolve (Fig. 2), and why contorted vesicles remain for longer (Fig. 4(a, c)).

Implications for tuffisite longevity

Our results provide a framework for understanding sintering of ash particles at high fluid pressures. Importantly, sintering was found to evolve at different rates, depending on pressure and temperature conditions and particle size. Such complexities are likely to be relevant in natural tuffisite veins, because volatile elements are thought to migrate through them after their formation (Berlo et al. 2013; von Aulock et al. 2013; Castro et al. 2014). Indeed, the particles in veins will equilibrate with the vein water pressure over the diffusion timescale. In the case where diffusion is rapid, sintering will progress in water equilibrium, as modeled by our experiments. Our analysis shows that we can predict sintering dynamics in scenarios where hydration precedes thorough sintering by using the viscosity at equilibrium water solubility in the low capillary Peclet number regime, and when particles are not monodisperse (given by $\overline{R}$)—conditions relevant to tuffisite closure.

Our model predicts that the porosity of tuffisite veins will decrease substantially as ash within them sinters to glass. Figure 8 shows that the porosity of the sintering ash drops over a fairly short dimensionless time window: rapid decrease in porosity begins only once $t \gtrsim 0.5\lambda_s$, and the final, fully dense value is reached by $t \approx 2\lambda_s$. Consequently, $t = \lambda_s$ is a useful approximate measure for the timescale of densification and, therefore, of the timescale over which tuffisite veins are expected to seal and become impermeable. In terms of dimensional variables, the sealing time depends on temperature and pressure (via their control on H_2O concentration and viscosity) and on the size of the ash particles (Eq. 1). To illustrate the variation in sealing time, we calculate λ_s as a function of depth in a magma-filled conduit (Fig. 9). The equilibrium solubility C_e was calculated as a function of depth, via Eq. 5, for T = 700, 800, and 900 °C; pressure was calculated assuming hydrostatic conditions and a constant density of 2000 kg m^{-3}. From this, η_e was calculated as a function of depth after Hess and Dingwell (1996). Particle sizes were fixed at either 10 μm (Fig. 9(a)) or 100 μm (Fig. 9(b)), and λ_s was calculated from Eq. 1. Using these simplifying assumptions, we find that for rhyolite at 800 °C, the timescale for sintering of fine ash (10 μm) to dense glass is less than a few minutes throughout most of the conduit. In contrast, cold, coarse rhyolitic ash at depths less than ~2 km takes hours to sinter (Fig. 9).

Figure 9 also plots the diffusion timescale λ_d for the same conditions, assuming diffusivity at equilibrium solubility. For a given depth, temperature, and particle size, if $\lambda_d < \lambda_s$, then Pc < 1. Our experiments were run in the low Peclet number regime; hence, our results are valid for Pc < 1. Furthermore, our experiments were run using natural materials at conduit conditions, so our results can be applied directly to the natural case, with no further scaling, in this regime. Our results show that for a given temperature, smaller particles spend more time in the shallow conduit in the low Pc regime.

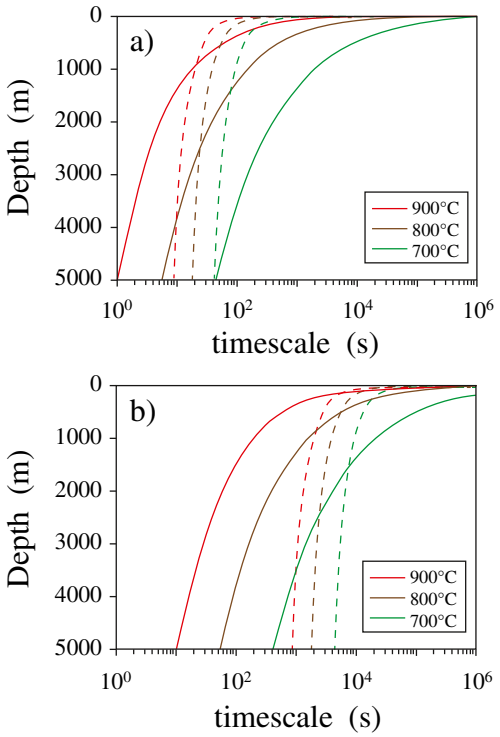

Fig. 9 Sintering timescales for (a) 10-μm and (b) 100-μm particles as functions of depth in a conduit filled with rhyolite at 700° (green curve), 800° (brown curve), or 900 °C (red curve). Also shown are the diffusion timescales for the same temperatures (dashed curves). The intersection between each pair of timescale curves represents Pc = 1. Conditions for Pc < 1 are met when the diffusion curve is to the left of the sintering curve

In Fig. 10, we present a regime plot that shows the position of the Pc = 1 curve in temperature–depth space, for particles of different radius. This plot can be used to determine the approximate conditions under which the analysis presented in this work can be applied to the natural case. For each line, the low Peclet number regime is towards lower temperature and shallower depth. For example, for magma at 800 °C and 3000-m depth, a particle of 10-μm radius will sinter such that Pc = 1, so our analysis can be applied. We can also see that any smaller particle will sinter in the Pc < 1 regime, as will a particle of 10 μm at lower temperature or shallower depth; our analysis therefore applies in all of these cases. By contrast, sintering of particles of 1-mm radius at 750 °C and 1000-m depth will be in the Pc > 1 regime. Consequently, diffusion will occur slowly compared with sintering, and our analysis cannot be assumed to be valid. Note the additional condition that our analysis is only valid for particles that are either hydrating or have water content that is approximately in equilibrium with the pressure and temperature conditions.

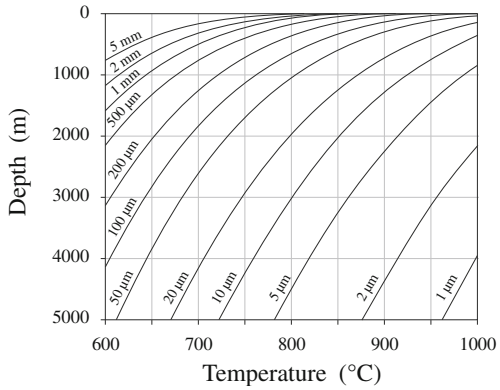

Fig. 10 Regime plot showing the position of the Pc = 1 curve in temperature–depth space for particles of different radius. The framework that we present for estimating sintering time is valid for sintering in the low Peclet number regime; this figure can be used to identify conditions that satisfy that requirement. For any curve, particles of the corresponding size will sinter in the low Peclet number regime if the temperature and depth plot to the left of the curve. Equivalently, for any given temperature and depth, particle sizes for which the corresponding curve passes to the right will sinter in the low Peclet number regime. For example, at 800 °C and 3000-m depth, particles of 10-μm radius or smaller will sinter in the Pc < 1 regime

A substantial decrease in porosity does not necessarily cause a decrease in the flow of gas through a tuffisite vein, because permeability may still be high, depending on the tortuosity of the connected pore space (e.g., Saar and Manga 1999). While we do not explicitly measure the permeability of the sintered samples, Wadsworth et al. (2016a) and Wright and Cashman (2014) showed that the permeability of a welding pack of particles or a welding ignimbrite will decrease as porosity decreases. This process was investigated in more detail by Wadsworth et al. (2017b), who tracked permeability evolution with time in polydispersive sintering systems. They showed that the time required for permeability to be reduced to 0 is the same as the sintering timescale (λ_s). Those authors found that the system permeability remains within an order of magnitude of the initial value up until ~$0.3\lambda_s$, and then decays rapidly by more than five orders of magnitude between $0.3\lambda_s$ and λ_s.

We observe that, when particles are only slightly to partially sintered (Phases 1–3), channels in the porous network can be traced visually through the sample, and hence the sample remains permeable. With time, those long-range channels seal off, and relaxation of the contorted vesicles creates spherical vesicles. Spherical to nearly spherical vesicles are isolated, such that gas could not flow between them; hence, samples that contain only spherical bubbles (i.e., at Phase 4) can be considered impermeable. At $\eta_e = 10^6$ Pa s, we thus infer that sintering created impermeable samples in about 10 min (Fig. 6). In contrast, at $\eta_e = 10^{7.5}$ Pa s, samples potentially remain permeable for more than 60 min. At relatively low viscosities, therefore, our results suggest that gas can flow through veins for only about 10–20 min. If low viscosity magma-containing veins thus ascended at a rate of 0.5 m s^{-1} (a reasonable assumption for the ascent of Chaitén magma while it simultaneously erupted and effused; Castro and Dingwell 2009), it would rise only ~300–600 m before the veins sealed. In contrast, the same magma with a viscosity of $\geq 10^7$ Pa s would remain permeable for > 60 min, allowing it to degas while rising > 1800 m. Given that, as magma rises, solubility drops, viscosity increases, and sintering timescale becomes longer, fractures that develop in the upper few kilometers of the conduit may be able to rise all the way to the surface before they seal.

Natural tuffisites can contain textural complexity not captured by our model system. Namely, clasts in partially welded tuffisites are often internally vesiculated (e.g., Castro et al. 2012; Saubin et al. 2016), exhibit evidence of internal densification of a previously vesicular clast (e.g., Castro et al. 2014; Saubin et al. 2016), or exhibit evidence of shear strain (e.g., Tuffen and Dingwell 2005). Tuffisites may also form in vesicular (Castro et al. 2012) or crystalline (Kendrick et al. 2016) magma and are not necessarily hosted in dense obsidian. In these cases, the densification timescales may be modified by syn-sintering bubble nucleation and bubble growth in large clasts, shear deformation of the welding tuffisite, and the presence of crystals in the groundmass. Our model therefore represents the scenario in which both the host and clast-fill are dominantly glassy.

Conclusions

The textural evolution of ash particle sintering under the action of surface tension follows the same trend for all temperature and pressure conditions, and for different ash size distributions. The rate of sintering is given by the sintering timescale λ_s (Eq. 1), which depends on the viscosity and size of the sintering particles. The porosity of a sintering pack of ash particles begins to drop appreciably around $0.5\lambda_s$ after the onset of sintering and reaches its final value at around $2\lambda_s$; permeability has been shown to drop from near its initial value to negligible over the interval $0.3\lambda_s$ to λ_s (Wadsworth et al. 2017b). The timescale over which an ash-filled crack is able to transport gas can therefore be computed if pressure, temperature, and particle size are known or can be estimated.

Our experiments were run under hydrating conditions, largely in the low Peclet number regime (Eq. 6), in which diffusion time is short compared with sintering time. Consequently, the sintering timescale is set by the viscosity under equilibrium H_2O solubility, and our results are relevant to sintering under conditions of equilibrium or near-equilibrium H_2O content. Our analysis can therefore be applied under low Peclet number conditions, which are favored by smaller particles, at shallower depth, and at lower temperatures. For reasonable estimates of natural magmatic conduits, low Peclet number conditions are

met in the upper few kilometers. We nonetheless expect that conditions in natural tuffisite veins may sometimes lead to sintering under high Peclet number and/or dehydrating conditions. Our analysis cannot be applied under such conditions, and further experimental work is required to characterize sintering behavior in those regimes.

Acknowledgements Jérémie Vasseur is warmly thanked for the discussion throughout. We thank two anonymous reviewers for their insights, which have improved the manuscript.

Funding information JEG was partially supported by a grant from the National Science Foundation (EAR–1348050). EWL and JPC acknowledge support from the UK Natural Environment Research Council via grant NE/N002954/1.

References

Bagdassarov N, Dorfman A, Dingwell DB (2000) Effect of alkalis, phosphorus, and water on the surface tension of haplogranite melt. Am Mineral 85:33–40

Berlo K, Tuffen H, Smith VC, Castro JM, Pyle DM, Mather TA, Geraki K (2013) Element variations in rhyolitic magma resulting from gas transport. Geochim Cosmochim Acta 121:436–451

Blank JG, Stolper EM, Carroll MR (1993) Solubilities of carbon dioxide and water in rhyolitic melt at 850 °C and 750 bars. Earth Planet Sci Lett 119:27–36

Cabrera A, Weinberg RF, Wrigh HMN, Zlotnik S, Cas RAF (2011) Melt fracturing and healing: a mechanism for degassing and origin of silicic obsidian. Geology 39:67–70

Castro JM, Dingwell DB (2009) Rapid ascent of rhyolite magma at Chaitén volcano. Nature 461:780–783

Castro JM, Cordonnier B, Tuffen H, Tobin MJ, Puskar L, Martin MC, Bechtel HA (2012) The role of melt-fracture degassing in defusing explosive rhyolite eruptions at Volcán Chaitén. Earth Planet Sci Lett 333–334:63–69

Castro JM, Bindeman IN, Tuffen H, Schipper CI (2014) Explosive origin of silicic lava: textural and δD–H_2O evidence for pyroclastic degassing during rhyolite effusion. Earth Planet Sci Lett 405:52–61

Dobson PF, Epstein S, Stolper EM (1989) Hydrogen isotope fractionation between coexisting vapor and silicate glasses and melts at low pressure. Geochim Cosmochim Acta 53:2723–2730

Eichelberger JC, Carrigan CR, Westrich HR, Price RH (1986) Non-explosive silicic volcanism. Nature 323:598–602

Gardner JE (2007) Heterogeneous bubble nucleation in highly viscous silicate melts during instantaneous decompression from high pressure. Chem Geol 236:1–12

Gardner JE, Ketcham RA (2011) Bubble nucleation in rhyolite and dacite melts: temperature dependence of surface tension. Contrib Mineral Petrol 162:929–943

Gardner JE, Webster JD (2016) The impact of dissolved CO_2 on bubble nucleation in water-poor rhyolite melts. Chem Geol 420:180–185

Giordano D, Dingwell DB (2003) Non-Arrhenian multicomponent melt viscosity: a model. Earth Planet Sci Lett 208:337–349

Giordano D, Russell JK, Dingwell DB (2008) Viscosity of magmatic liquids: a model. Earth Planet Sci Lett 271:123–134

Gonnermann H, Manga M (2003) Explosive volcanism may not be an inevitable consequence of magma fragmentation. Nature 426:432–435

Hess K-U, Dingwell DB (1996) Viscosities of hydrous leucogranitic melts: a non-Arrhenian model. Am Mineral 81:1297–1300

Jaupart C, Allegre CJ (1991) Gas content, eruption rate and instabilities of eruption regime in silicic volcanoes. Earth Planet Sci Lett 102:413–429

Kendrick JE, Lavallée Y, Varley NR, Wadsworth FB, Lamb OD, Vasseur J (2016) Blowing off steam: tuffisite formation as a regulator for lava dome eruptions. Front Earth Sci 4:41

Liu Y, Zhang Y, Behrens H (2005) Solubility of H_2O in rhyolitic melts at low pressure and a new empirical model for mixed H_2O-CO_2 solubility in rhyolitic melts. J Volcanol Geotherm Res 143:219–235

Lowenstern JB, Pitcher BW (2013) Analysis of H_2O in silicate glass using attenuated total reflectance (ATR) micro-FTIR spectroscopy. Am Mineral 98:1660–1668

Michaut C, Bercovici D, Sparks RSJ (2009) Ascent and compaction of gas rich magma and the effects of hysteretic permeability. Earth Planet Sci Lett 282:258–267

Quane SL, Russell JK, Friedlander EA (2009) Time scales of compaction in volcanic systems. Geology 37:471–474

Richet P (1984) Viscosity and configurational entropy of silicate melts. Geochim Cosmochim Acta 48:471–483

Russell JK, Giordano D, Dingwell DB (2003) High-temperature limits on viscosity of non-Arrhenian silicate melts. Am Mineral 8:1390–1394

Saar MO, Manga M (1999) Permeability–porosity relationship in vesicular basalts. Geophys Res Lett 26:111–114

Saubin E, Tuffen H, Gurioli L, Owen J, Castro JM, Berlo K, McGowan EM, Schipper CI, Wehbe K (2016) Conduit dynamics in transitional rhyolitic activity recorded by tuffisite vein textures from the 2008–2009 Chaitén eruption. Front Earth Sci 4:59

Schipper CI, Castro JM, Tuffen H, James MR, How P (2013) Shallow vent architecture during hybrid explosive–effusive activity at Cordón Caulle (Chile, 2011–12): evidence from direct observations and pyroclast textures. J Volcanol Geotherm Res 262:25–37

Stasiuk MV, Barclay J, Carroll MR, Jaupart C, Ratté JC, Sparks RSJ, Tait SR (1996) Degassing during magma ascent in the Mule Creek vent (USA). Bull Volcanol 58:117–130

Tuffen H, Dingwell DB (2005) Fault textures in volcanic conduits: evidence for seismic trigger mechanisms during silicic eruptions. Bull Volcanol 67:370–387

Tuffen H, Dingwell DB, Pinkerton H (2003) Repeated fracture and healing of silicic magma generate flow banding and earthquakes? Geology 31:1089–1092

Vasseur J, Wadsworth FB, Lavallée Y, Hess K-U, Dingwell DB (2013) Volcanic sintering: timescales of viscous densification and strength recovery. Geophys Res Lett 40:1–7

Von Aulock FW, Nichols ARL, Kennedy BM, Oze C (2013) Timescales of texture development in a cooling lava dome. Geochim Cosmochim Acta 114:72–80

Wadsworth FB, Vasseur J, Aulock FW, Hess KU, Scheu B, Lavallée Y et al (2014) Nonisothermal viscous sintering of volcanic ash. J Geophys Res Solid Earth 119:8792–8804

Wadsworth FB, Vasseur J, Scheu B, Kendrick JE, Lavallée Y, Dingwell DB (2016a) Universal scaling of fluid permeability during volcanic welding and sediment diagenesis. Geology 44:219–222

Wadsworth FB, Vasseur J, Llewellin EW, Schauroth J, Dobson KJ, Scheu B, Dingwell DB (2016b) Sintering of viscous droplets under surface tension. Proc Roy Soc A 472:20150780

Wadsworth FB, Vasseur J, Llewellin EW, Genareau K, Cimarelli C, Dingwell DB (2017a) Size limits for rounding of volcanic ash particles heated by lightening. J Geophys Res Solid Earth 122:1977–1989

Wadsworth FB, Vasseur J, Llewellin EW, Dobsan KJ, Colombier M, von Aulock FW, Fife JL, Wiemaier S, Hess K-U, Scheu B, Lavallée Y, Dingwell DB (2017b) Topographical inversions in coalescing granular media control fluid flow regimes. Phy Rev E 96:033113

Watkins JM, Gardner JE, Befus KS (2017) Nonequilibrium degassing, regassing, and vapor fluxing in magmatic feeder systems. Geology 45:183–186

Wessel P, Smith WH, Scharroo R, Luis J, Wobbe F (2013) Generic mapping tools: improved version released. EOS, Trans Am Geophys Un 94:409–410

Wright HM, Cashman KV (2014) Compaction and gas loss in welded pyroclastic deposits as revealed by porosity, permeability, and electrical conductivity measurements of the Shevlin Park tuff. Geol Soc Am Bull 126:234–247

Zhang Y, Ni H (2010) Diffusion of H, C, and O components in silicate melts. Rev Mineral Geochem 72:171–225

Zhang Y, Belcher R, Ihinger PD, Wang L, Xu Z, Newman S (1997) New calibration of infrared measurement of dissolved water in rhyolitic glasses. Geochim Cosmochim Acta 61:3089–3100